

Article

Comparison of Planetary Boundary Layer Height Derived from Lidar in AD-Net and ECMWFs Reanalysis Data over East Asia

Zhijuan Zhang *, Ling Mu and Chen Li

College of Environmental Science and Engineering, Taiyuan University of Technology, Taiyuan 030024, China

* Correspondence: zhangzhijuan@tyut.edu.cn

Abstract: The planetary boundary layer height is a very important parameter in the atmosphere because it determines the range where the most effective dispersion processes take place, and it serves as a medium for the vertical transport of heat, moisture, and pollutants. The accurate estimation of boundary layer height (BLH) is vital for air pollution prediction. In this paper, the BLH estimated by AD-Net was compared with that from the ECMWFs over East Asia from September 2015 to August 2018. A continuous 24 h BLH estimation from AD-Net generally matched with the aerosol vertical structures. Diurnal and seasonal variation and spatial variation of BLH can also be shown, suggesting the good performance of AD-Net BLH. The comparison of seasonal mean BLH between AD-Net and ECMWFs was conducted at 20 lidar sites. On average, there was an underestimation of the ECMWFs, mostly in summer and winter. A significant disagreement between AD-Net and the ECMWFs was noted, especially over coastal areas and mountain areas. In order to investigate the difference between them, two BLHs were compared under different land cover types and climate conditions. In general, the BLH of the ECMWFs was less than that of AD-Net over most of the land cover types in summer and winter. The smallest differences (0.26 km) existed over water surfaces in winter compared with AD-Net, and the largest underestimation (1.42 km) occurred over grassland surfaces in summer. Similarly, all the BLHs of the ECMWFs were lesser than those of AD-Net under different climatological conditions in summer and winter. The mean difference between AD-Net BLH and ECMWFs BLH was 1.05, 0.71, and 0.48 km for arid regions, semi-arid and semi-wet regions, and wet regions, respectively. The largest underestimation occurred over arid regions in winter, with a value of 1.42 km. The smallest underestimation occurred over wet regions, with a value of 0.27 km. The present research provides better insight into the BLH performance in the ECMWFs reanalysis data. The new continuous PBL dataset can be used to improve the model parameterization of PBL and our understanding of the atmospheric transport of pollutants which affect air quality and human health.



Citation: Zhang, Z.; Mu, L.; Li, C. Comparison of Planetary Boundary Layer Height Derived from Lidar in AD-Net and ECMWFs Reanalysis Data over East Asia. *Atmosphere* **2022**, *13*, 1976. <https://doi.org/10.3390/atmos13121976>

Academic Editors: Zhengqiang Li, Zhongwei Huang, Chi Li, Kai Qin, Han Wang, Tianhe Wang and Jie Luo

Received: 20 October 2022

Accepted: 23 November 2022

Published: 26 November 2022

Publisher's Note: MDPI stays neutral with regard to jurisdictional claims in published maps and institutional affiliations.



Copyright: © 2022 by the authors. Licensee MDPI, Basel, Switzerland. This article is an open access article distributed under the terms and conditions of the Creative Commons Attribution (CC BY) license (<https://creativecommons.org/licenses/by/4.0/>).

Keywords: planetary boundary layer; boundary layer height; lidar; ECMWFs; aerosol

1. Introduction

The planetary boundary layer (PBL) is the lowest part of the troposphere and is directly influenced by the Earth's surface through the exchange of heat, momentum, and moisture [1,2]. It determines the vertical extent of turbulent mixing, vertical diffusion, and convective transport within the PBL, and it is also a primary determinant of cloud type and coverage that affects the Earth's radiation budget [3]. The important roles of the PBL in weather and climate have long been recognized. In order to better characterize the structure of the PBL, the concept of boundary layer height (BLH) is commonly used [4,5]. Therefore, it is critical to obtain an accurate BLH, since it is important for air quality, weather forecasting, and the assessment of regional climate change.

Traditionally, the BLH is diagnosed using the vertical profiles of temperature, humidity, and wind from radiosonde observation [4–6]. The bulk Richardson number (Ri) method [7]

can also be used to estimate the BLH. New data sources such as ground-based lidar [8,9] instruments, sodar [10], ceilometer [11], aircraft sounding [12], and space-borne lidar [13–15] can be relied on to retrieve the BLH. In addition, the structure of turbulence can also be determined from optical measurements performed on ground-based telescopes [16–19].

It is noted that products on the global climatology of BLHs are available freely from the European Centre for Medium-Range Weather Forecasts (ECMWFs). A comparison of seasonally averaged BLHs derived from fine-resolution sounding observations and ECMWFs reanalysis over China showed good agreement on average, despite the pronounced inconsistencies in some regions [6]. However, the ECMWFs reanalysis products perform significantly worse than those from the Cloud-Aerosol Lidar and Infrared Pathfinder Satellite Observations (CALIPSOs) lidar-based BLH over the oceans and coastal areas in China. The BLHs from the ECMWFs are greater than those from CALIPSOs over North China in spring and summer. The majority of the ECMWFs BLHs are within 25% of the estimates derived from CALIPSOs in autumn. The comparison of CALIPSOs and ECMWFs BLHs under different land-cover conditions reveals that the BLH estimated by the CALIPSOs backscatter climatology is higher over ocean and forest surfaces and lower over grassland and bare land surfaces in spring and summer [14]. Although many researchers have used the ECMWFs BLH, its precision is still poor because the verification of the BLH by direct observations is rare. Additionally, climate modelers are constantly searching for new opportunities to verify model outputs.

BLH derived from ground-based lidar can be used for comparison and validation with others. Ground-based lidar has the advantage of continuous tracing and thus avoids confusion with elevated layers. BLH is determined using a combination of the averaging variance method and the high-resolution gradient method from lidar backscatter measurements [8]. Additionally, it also can be detected from micropulse lidar (MPL)-measured backscatter [9]. In addition, AD-Net is used for the validation of EarthCARE satellite observation and data assimilation to evaluate emissions of air pollution and dust aerosols in East Asia [20,21]. Therefore, AD-Net BLHs can be used for comparison with the ECMWFs reanalysis data in this study.

Here, the seasonal mean BLH derived from the National Institute for Environmental Studies' (NIESs') ground-based lidar in the Asian Dust and Aerosol Lidar Observation Network (AD-Net) is directly used to perform comparisons and further validations with the BLH from the ECMWF ERA-Interim fields from September 2015 to August 2018 in this study. This paper is arranged as follows. The details of the datasets are given in Section 2. In Section 3, a comparison of BLHs obtained from AD-Net and the ECMWF in summer and winter and under different land cover types and climate conditions is presented. The conclusion and discussion are presented in Sections 4 and 5, respectively.

2. Materials and Methods

2.1. BLH Derived from AD-Net

AD-Net is a lidar network for the continuous observation of vertical distributions of Asian dust and other aerosols (including industrial, forest fire, volcanic) in East Asia, and for studying the impacts of aerosols on the air quality and atmosphere environment. Gaining a quantitative understanding of Asian dust emissions, transport, and deposition, the long-term variations of Asian dust and anthropogenic aerosols, and the effects of aerosols on human health, vegetation, and radiation is objective of this network. Officially, there are 20 sites with automatic lidars over East Asia, mainly situated in Japan. The standard lidar in AD-Net is a two-wavelength polarization-sensitive (532 nm) Mie-scattering lidar [22]. The measured data are transferred to the AD-Net in real-time and processed automatically. Data from AD-Net are strictly managed and quality-assured (<http://www-lidar.nies.go.jp/AD-Net/ncdf/>, accessed on 23 November 2022).

Figure 1 shows the topography of 20 AD-Net lidar stations in AD-Net [23,24], i.e., Chiba (CHB), Fukue (FKE), Fukuoka (FKO), Hedo (HED), Gosan Jeju (JEJ), Matsue (MTS), Nagasaki (NGS), Niigata (NIG), Osaka (OSK), Phimai (PHM), Seoul (SEO), Sendai (SND),

Sainshand (SNS), Sapporo (SPR), Tsukuba (TKB), Tokyo (TKO), Toyama (TYM), Ulaanbaatar (ULN), Ulsan (ULS), and Zamynnuud (ZMY). The basic parameters derived are the attenuated backscattering coefficients (ABCs) at 532 nm and 1064 nm, and the volume depolarization ratio at 532 nm. Extinction coefficient estimates for non-spherical and spherical aerosols are also derived with this method using the backscattering and depolarization ratio [25,26].

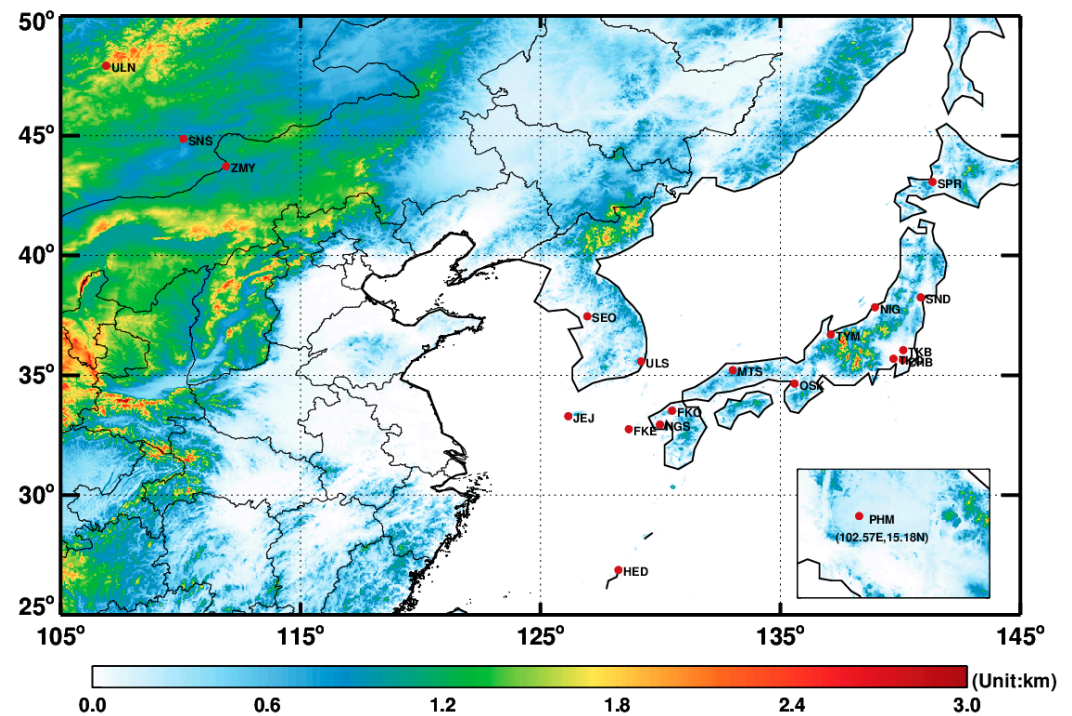


Figure 1. The location of AD-Net lidar stations (the red solid circle). The color represents surface elevation.

BLH is identified using the vertical gradient of the ABC at 532 nm with the method used in Sugimoto et al. [22]. Due to the fact that the aerosols have the largest loading in the PBL, the gradient of the backscattering signal decreases rapidly at the top of the PBL. Therefore, the BLH is defined as the height at which the gradient of the ABC at 532 nm reaches a minimum value. The minimum value was set empirically. When this criterion is satisfied, the layer is identified as an aerosol layer, and the top of the layer is identified as the BLH [20]. AD-Net provides the near-real-time mixing layer height (MLH) since 2001 at 20 sites. The vertical and temporal resolution of AD-Net lidar is 30 m and 15 min, respectively. Here, the MLH was regarded as the BLH and was compared with the ECMWFs BLH.

2.2. BLHs from ECMWFs

The ECMWFs' core mission is to produce numerical weather forecasts and monitor the Earth system, as well as to carry out scientific and technical research to improve forecasting skills and to maintain an archive of meteorological data. It provides air quality analysis, atmospheric composition monitoring, and climate monitoring. Global climatology BLHs are a small part of their products and are important for understanding the physical process in the boundary layer. The ECMWFs models produce BLHs by means of the bulk Richardson number method. The bulk Richardson number is defined as the ratio of stability to vertical wind shear, which is expressed as:

$$Ri(z) = \frac{\left(\frac{g}{\theta_{vs}}\right)(\theta_{vz} - \theta_{vs})(z - z_s)}{(u_z - u_s)^2 + (v_z - v_s)^2 + (bu_*^2)} \quad (1)$$

where g is the acceleration due to gravity, θ is the potential temperature, θ_{vs} and θ_{vz} are the virtual potential temperature at surface and at height z above ground level, respectively, u and v are the components of wind speed, and u^* is the surface friction velocity, while b is a coefficient to be determined [7]. Previous theoretical and laboratory studies (e.g., [2]) suggested that when Ri is smaller than the critical value (~ 0.25), the laminar flow becomes unstable. Thus, the lowest-level z at which the interpolated Ri crosses the critical value of 0.25 is referred to as the BLH in this study, similar to the criteria used by Seidel et al. [12,27–31]. This method works well for both stable and convective boundary layers [27]. However, it may reach this critical value at a height somewhat below the BLH defined by other means [32].

The ECMWFs has provided monthly mean BLHs with 0.125×0.125 latitude–longitude resolution at the global scale from 1979 to the present. Here, the BLH from September 2015 to August 2018 over East Asia was used for comparison with the AD-Net BLH.

3. Results

It was proved that the BLH from CALIPSO is strongly correlated with that from ground-based lidar [14]. Therefore, the BLH derived using the maximum standard variance method is reliable. Figure 2 shows a series of cases of BLH estimation using the ABCs profile and extinction profile in August 2018. The BLHs from the AD-Net product and the BLHs derived using the maximum standard variance method [14] are shown as a dotted line and dashed line, respectively. The two methods are both based on the aerosol backscatter. Close agreement was observed between them, which suggested the good performance of the AD-Net BLH.

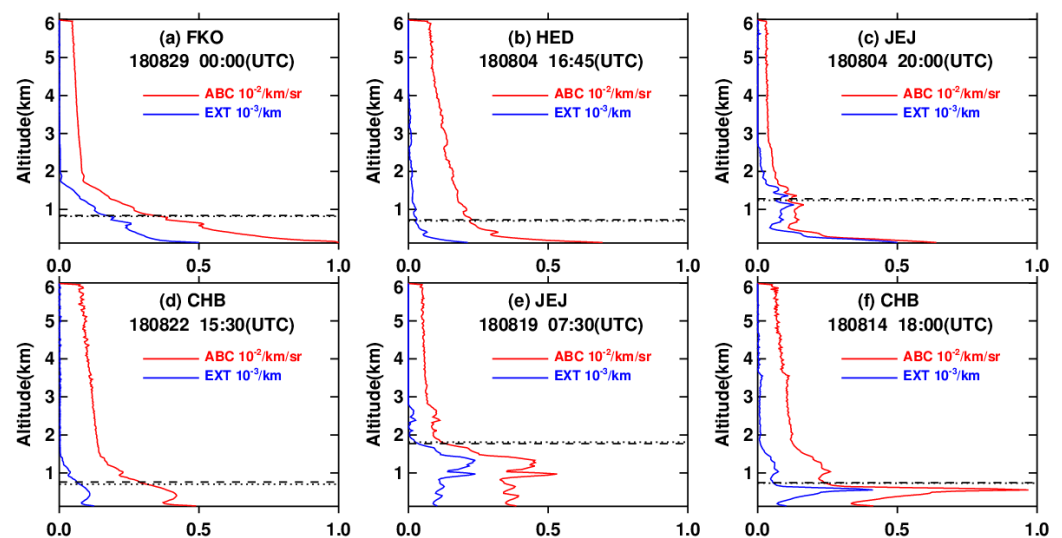


Figure 2. Profile of the attenuated backscatter coefficient (ABC) at 532 nm and extinction coefficient profiles (EXT) using the Fernald inversion on (a) 29 August 2018 at the site of FKO, (b) 4 August 2018 at the site of HED, (c) 4 August 2018 at the site of JEJ, (d) 22 August 2018 at the site of CHB, (e) 19 August 2018 at the site of JEJ and (f) 14 August 2018 at the site of CHB. The BLH from CALIPSO and Lidar is shown in dotted line and dashed line, respectively. The vertical and time resolution is 30 m and 15 min, respectively.

Figure 3 shows a case study of a continuous 24 h AD-Net ground-based lidar profile, which contains the ABC at 532 nm (a), the ABC at 1064 nm (b), the volume depolarization ratio (d), and the color ratio (d) distributions observed from AD-Net lidar at the MTS station, with the BLH (gray solid circle) on 7 August 2018. The depolarization ratio, which is a parameter sensitive to the nonsphericity of the scatters, is useful for identifying mineral dust aerosols and in discriminating between water and ice clouds [22]. The color ratio between 1064 nm and 532 nm backscatter is efficient in detecting falling droplets which

evaporate before reaching the surface [33]. Clear aerosol signature layers extending from 120 m to 1 km and the boundary layer cloud at the top of the boundary layer are shown. In order to minimize the influence of the clouds on the BLH determination, all of the lidar measurements with clouds were excluded for further analyses. The BLH derived from AD-Net lidar generally matched with the aerosol vertical structures. In addition, a diurnal variation of BLH can be clearly seen. During a diurnal cycle, the BLH is typically shallow (about 900 m) at night due to the strong near-surface stability, and well-developed and reaching a maximum of 1.18 km in the afternoon.

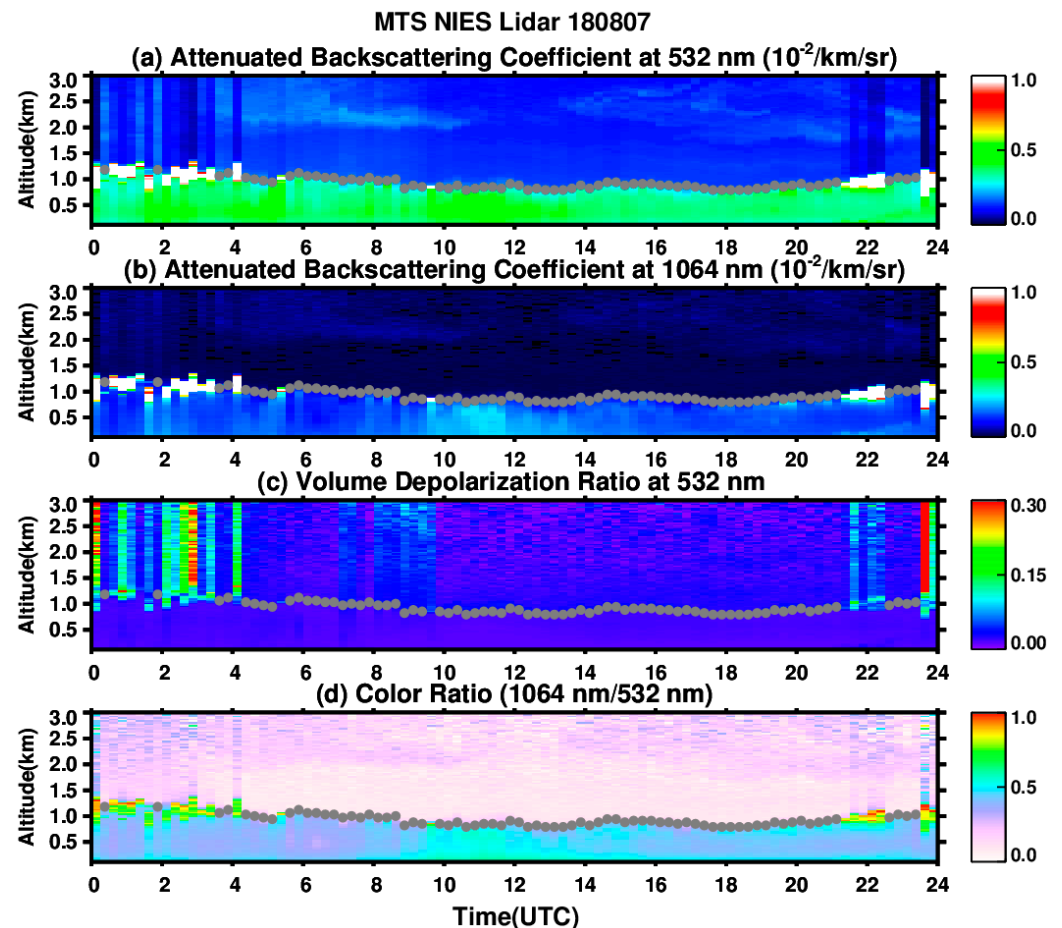


Figure 3. (a) Attenuated backscatter coefficient at 532 nm, (b) attenuated backscatter coefficient at 1064 nm, (c) volume depolarization ratio at 532 nm, and (d) color ratio (1064 nm/532 nm) observed from AD–Net ground-based lidar on 7 August 2018. The gray solid circle indicates AD–Net lidar BLH.

Figure 4 shows the mean seasonal geographic distribution of the BLH concerning the location of each lidar site. It can be clearly seen that the BLHs exhibit large spatial and seasonal variations. On average, more intense solar radiation reaching the surface in summer favors the PBL development on the land, but the development of the PBL is typically suppressed due to the smaller amount of solar radiation received at the surface [2]. For ocean areas, the situation is entirely different due to its relatively large heat capacity. The mean BLH over inland areas (including the ULN, SNS, ZMY, and PHM sites) was larger than that over ocean areas (including the JEJ, FKE, and HED sites) in summer (see Table 1). However, the opposite distribution was observed in winter. Additionally, this indicated that over coastal areas, the BLH in winter was greater than that in summer, which was consistent with Liu et al. [14]. A possible explanation is that the sea–land wind contributes to the development of the PBL height over the coastal areas. The highest BLH (2.23 km) was seen at the ZMY site (at the border of Mongolia, surface elevation of 962 m) in summer

(June, July, and August), and the lowest BLH value (0.77 km) occurred at the TYM site (on the west coast of Japan) in winter (December, January, and February).

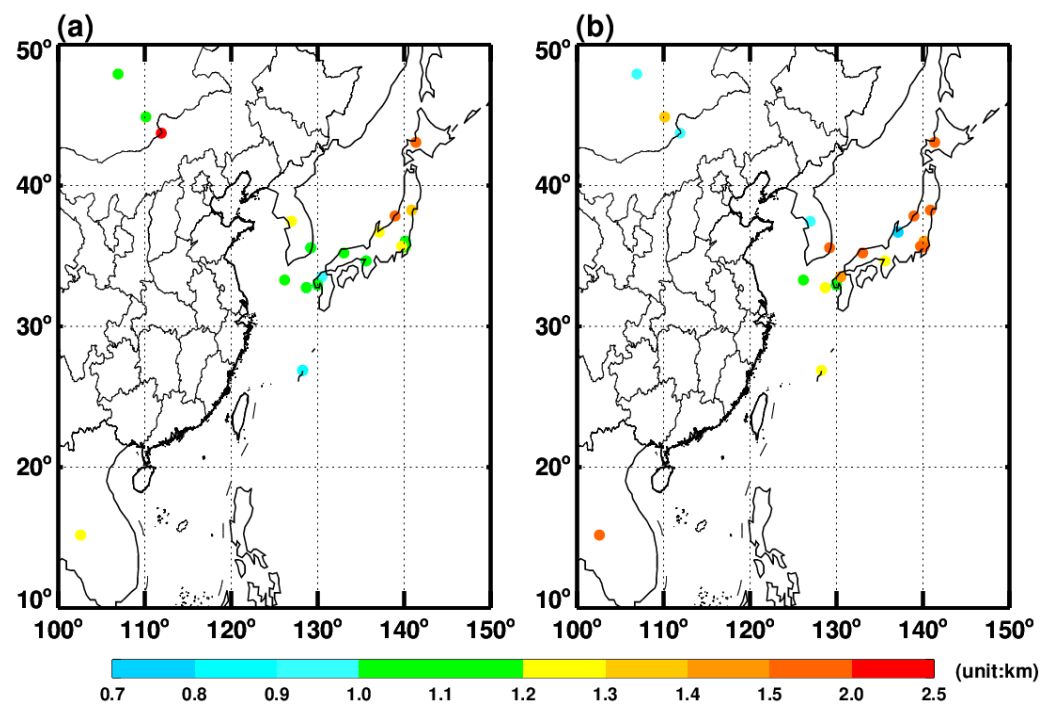


Figure 4. Spatial patterns of 3-year seasonal mean BLH for 20 sites in AD-Net over East Asia from the AD-Net for summer (a) and winter (b).

Table 1. BLH derived from AD-Net over inland and ocean area.

	Summer	Winter
Inland	1.44	1.19
Ocean	1.01	1.22

A comparison between BLHs from AD-Net and the ECMWFs was conducted at 20 lidar sites, as shown in Figure 5. In terms of similar spatial distribution of BLH, discrepancies between them still existed. Compared with AD-Net BLH, there was an underestimation of the ECMWFs BLH both in summer and winter, except over the ocean in winter. The ECMWFs BLH was in close agreement with the AD-Net BLH at the JEJ, MTS, and NGS sites in winter with a relative difference smaller than 10% (Figure 6b). The spatial distribution of the BLH revealed a tendency for higher BLHs over high-elevation regions, consistent with the dependence on elevation reported in the United States [27]. However, the BLH from the ECMWFs was severely underestimated at high-surface elevation sites (including ULN, ZMY, and SNS in Mongolia), especially in winter, with a relative difference around 80% (Figure 6b).

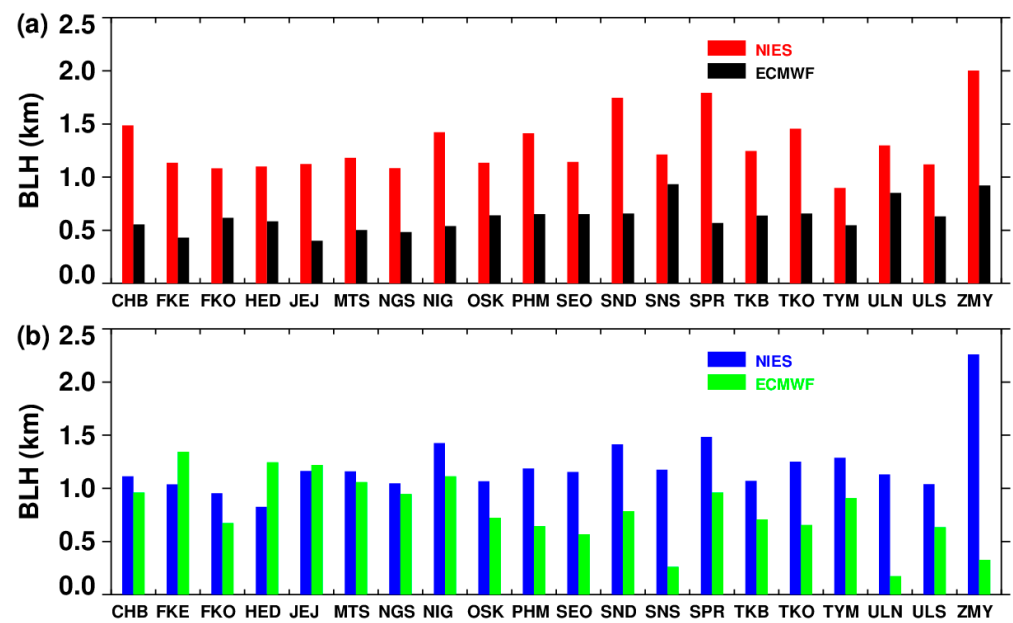


Figure 5. Comparison of the AD-Net PBL and ECMWFs PBL for 20 sites from AD-Net for summer (a) and winter (b).

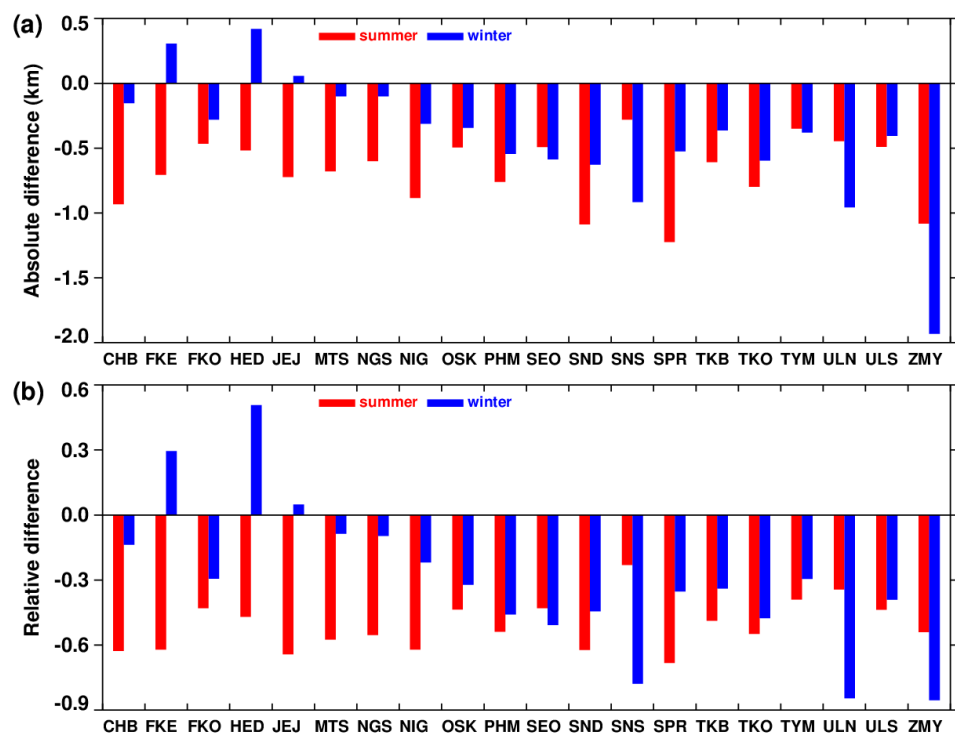


Figure 6. (a) Absolute difference, (b) relative difference in the BLH from AD-Net and ECMWFs for 20 sites in AD-Net.

As noted above, a seasonal disagreement was found in BLH climatology. Here, we continue to explore these seasonal biases quantitatively. The seasonally averaged absolute differences and relative differences between the AD-Net BLH and the ECMWFs BLH are presented in Figure 6a,b. The mean absolute difference was 0.68 km and 0.42 km in summer and in winter, respectively. Additionally, the relative difference was 0.51 and 0.30 in summer and in winter, respectively. The larger absolute difference in BLH was in summer because the BLH from the ECMWFs was uniformly underestimated compared to the AD-Net BLH. The poor estimation of BLH can mainly be attributed to the lower

BLH over land, especially for mountainous areas (see Table 2). However, large biases of the seasonal BLHs were most likely due to the different methods utilized based on radiosonde, ground-based lidar, and CALIPOs observations over one site in South Africa [34].

Table 2. Mean difference in BLH derived from AD-Net and ECMWFs (ECMWFs BLH minus AD-Net BLH) in summer and winter.

	Absolute Difference (km)		Relative Difference	
	Summer	Winter	Summer	Winter
Inland	−0.64	−1.09	−0.41	−0.73
Ocean	−0.65	0.26	−0.58	0.28
Coastal areas	−0.70	−0.37	−0.53	−0.30
Mountain	−0.60	−1.27	−0.37	−0.83

Next, we will analyze which land cover type and climate condition has the largest influence on the differences in the seasonal variation between the ECMWFs BLH and the AD-Net BLH. The vegetation types in China, as determined by MODIS at 0.05 degrees of spatial resolution, are plotted in Figure 7a, including 17 different surface types. Precipitation data from the University of East Anglia Climate Research Unit (CRU) global climate dataset at 0.5° latitude and longitude resolution were used as a proxy for climate state [35]. In this study, the monthly mean climatology was calculated relative to the average for the period of 1961–1990. The spatial distribution of precipitation is shown in Figure 7b. The annual mean precipitation ranges from 0 to 200, from 200 to 800, and over 800 mm yr^{−1} in arid regions, semi-arid and semi-wet regions, and wet regions, respectively.

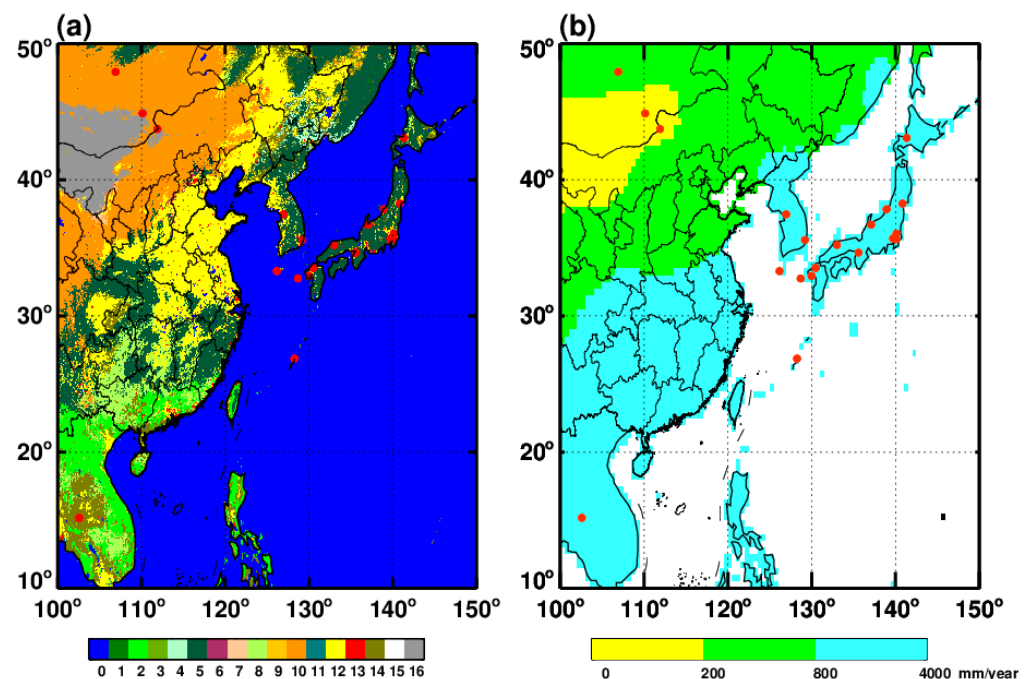


Figure 7. (a) Land cover distribution in 2011 from MODIS (0.05 degree) over East Asia. (b) Precipitation distribution averaged from 1961 to 1990. (0 = water, 1 = evergreen needleleaf, 2 = evergreen broadleaf, 3 = deciduous needleleaf, 4=deciduous broadleaf, 5 = mixed forests, 6 = closed shrubland, 7 = open shrublands, 8 = woody savannas, 9 = savannas, 10 = grasslands, 11=permanent wetlands, 12 = croplands, 13 = urban and built-up, 14 = cropland mosaic, 15 = snow and ice, 16 = bare or sparsely vegetated).

The seasonal mean values of the AD-Net BLH and the ECMWFs BLH under the condition of different land cover types are presented in Figure 8, and detailed differences

in summer and winter are listed in Table 3. We found that, in general, the BLHs of the ECMWFs were lower than those of AD-Net over most of the land cover types in summer and winter, except for over ocean areas in winter. The smallest differences existed over water surfaces in winter and bare surfaces in summer. Additionally, the largest differences occurred over grassland surfaces in winter, with the largest underestimation of 1.93 km compared to the AD-Net BLH, followed by 1.08 km over grassland surfaces in summer. Overall, the mean minimum and maximum differences occurred over water surfaces and grassland surfaces, respectively. These results are different from those of Liu et al. [14], who suggested that the largest differences occurred over bare land surfaces in summer with the largest overestimate (0.97 km), and over water surfaces in spring with the greatest underestimation (−0.91 km) compared with CALIPSOs. There are more land cover types in China due to its vast area, and different meteorological conditions along with its complex pollution conditions, which may lead to the above results.

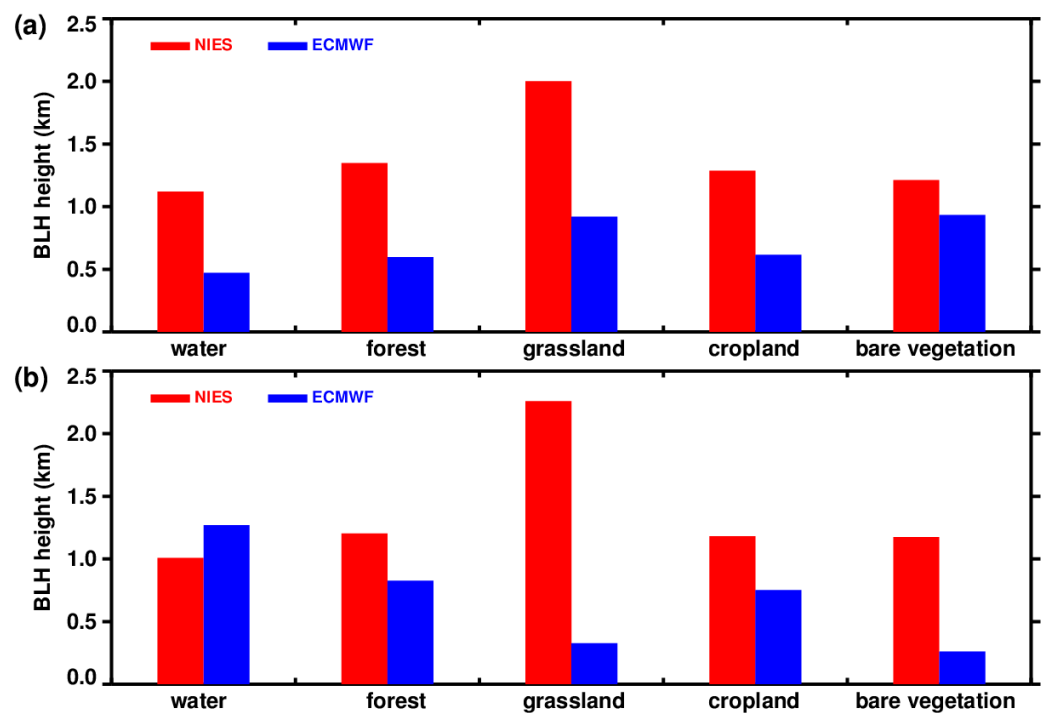


Figure 8. Comparison of AD-Net (red) and ECMWFs (blue) PBL in the case of different land cover types (water, forest, grassland, cropland, and bare vegetation) for summer (a) and winter (b).

Table 3. Seasonal differences in BLH between AD-Net and ECMWFs (ECMWFs PBL minus AD-Net PBL) given different land cover conditions.

	Water	Forest	Grassland	Cropland	Bare Vegetation
Summer	−0.65	−0.79	−1.08	−0.67	−0.28
Winter	0.26	−0.52	−1.93	−0.43	−0.91

The seasonal mean values of the AD-Net BLH and the ECMWFs BLH under different climatological conditions are presented in Figure 9, and detailed differences in summer and winter are listed in Table 4. We found that all the BLHs of the ECMWFs were lower than those of AD-Net under different climatological conditions in summer and winter. The largest underestimation occurred over arid regions in winter, with a value of 1.42 km. The smallest underestimation occurred over wet regions, with a value of 0.27 km. The mean difference between the AD-Net BLH and the ECMWFs BLH was 1.05, 0.71, and 0.48 km for arid regions, semi-arid and semi-wet regions, and wet regions, respectively. In wet regions,

the number of lidar stations was the largest, which may contribute to the minor difference between the AD-Net BLH and the ECMWFs BLH. Special attention should be paid to the fact that it is in arid regions that the relative difference in summer and in winter (0.74 km) was the largest, which meant that this region was the most sensitive in the related physical parameterization in the ECMWFs model.

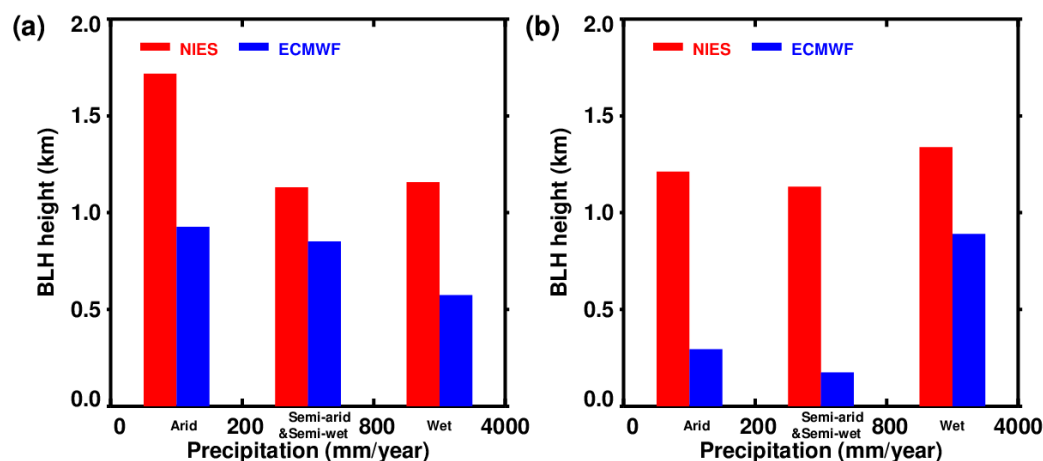


Figure 9. Comparison of AD-Net (red) and ECMWFs (blue) PBL in the case of different climate conditions (arid, semi-arid and semi-wet, and wet) for summer (a) and winter (b).

Table 4. Mean differences in BLH between AD-Net and ECMWFs (ECMWFs PBL minus AD-Net PBL) in summer and winter when given different climate conditions.

	Arid	Semi-Arid and Semi-Wet	Wet
Summer	−0.68	−0.45	−0.69
Winter	−1.42	−0.96	−0.27

4. Conclusions

In this paper, we compared the BLHs estimated by AD-Net and the ECMWFs over East Asia from September 2015 to August 2018. The present research provides better insight into the BLH performance in the ECMWFs reanalysis data.

The BLH determined by AD-Net was in close agreement with that calculated by Liu et al. [14], using the methods based on the aerosol backscatter. Additionally, a continuous 24 h BLH estimation from AD-Net generally matched with the aerosol vertical structures and the diurnal variation of the BLH is clearly shown, which suggests the good performance of the AD-Net BLH.

A comparison between seasonal mean BLH from AD-Net and the ECMWFs was conducted at 20 lidar sites. On average, there was an underestimation from the ECMWFs compared with AD-Net, both in summer and winter, except for over ocean areas in winter. A significant disagreement between the AD-Net BLH and the ECMWFs was noted over coastal areas and mountain areas. The absolute difference in BLH was larger in summer because the BLH from the ECMWFs was uniformly underestimated.

In general, the BLH of the ECMWFs was lower than that of AD-Net over most of the land cover types in summer and winter, except for over ocean areas in winter. The smallest differences existed over water surfaces in winter and bare surfaces in summer, and the largest differences occurred over grassland surfaces in summer, with the largest underestimation of 1.93 km compared with AD-Net. Overall, the mean minimum and maximum differences occurred over water surfaces and grassland surfaces, respectively.

All the BLHs of the ECMWFs were lower than those of AD-Net under different climatological conditions in summer and winter. The largest underestimation occurred

over arid regions in winter, with a value of 1.42 km. The smallest underestimation occurred over wet regions, with a value of 0.27 km. The mean difference between the AD-Net BLH and the ECMWFs BLH was of 1.05, 0.71, and 0.48 km for arid regions, semi-arid and semi-wet regions, and wet regions, respectively. The difference in absolute uncertainty of the two BLHs in summer and in winter (0.74 km) was the largest in arid regions, which meant that this region was the most sensitive in the related physical parameterization in the ECMWFs model.

5. Discussion

To the best of our knowledge, there have been a number of studies that have used remote sensing to generate the BLH. These studies have used different techniques to identify the top of the PBL. The first set of studies used the temperature difference at the top marine stratus or stratocumulus clouds and sea surface to estimate PBL depth [36]. Height-resolved temperature observations from limb sounders, however, have the potential for PBL depth detection. Due to the fact that the PBL top is often marked with a sharp decrease in aerosol scattering signals that can be detected from space [37], the second approach is to use these signals to estimate the BLH [14]. Additionally, refractivity profiles with high vertical resolution provide, by means of a space-borne global positioning system, radio occultation, making this approach attractive for PBL detection [38,39]. Their strengths and weaknesses are all different, owing to the different detection methods. It is noted that the BLH is not produced directly. Therefore, the quality of the related physical variables is vital for the accurate estimation of the BLH.

Many researchers have shown that dust events seem to be a possible reason for the great difference between the different estimations of the BLH [40,41]. Thus, it is necessary to screen the dust cases when a comparison is conducted. In order to identify the dust cases, it is the best solution for us to use the lidar observations. The volume linear depolarization ratio (VLDR), which can indicate the shape of atmospheric particles, is a key parameter to distinguish the aerosol types. The different aerosol types exhibit a clear difference in the VLDR. Due to this, the VLDR can be considered to identify the dust aerosols, together with the lidar return signal [28,42–46]. The identification of the dust case can be achieved by using the VLDR; that is, when the value of the layer is larger than the threshold of dust, the profile is considered to be affected by the dust aerosols, and then the profile is screened for the comparison of BLHs. On the other hand, during a diurnal cycle, the atmosphere boundary layer structure can be classified into three major regimes [2]: convective boundary layer (CBL), stable boundary layer (SBL), and residual layer (RL). Lidar has been used for tracking the evolution of the BLH by using aerosol backscatter as a tracer, assuming aerosol is generally well-mixed in the planetary boundary layer. However, the validity of this assumption in fact varies with atmospheric stability [47]. For example, the relationship of the heights of intense turbulent exchange and the corresponding temperature gradients in the boundary layer of the atmosphere are analyzed with the ground values of wind speed and vertical turbulent heat flow [48]. Therefore, it is necessary to compare the BLH under different atmosphere stratifications.

In coastal regions, the formation of a thermal internal boundary layer (TIBL) is a common boundary layer phenomenon. In the sunny daytime, the sea breeze will blow the stable or neutrally stratified air over the sea toward the land. The surface-heating effect and dynamic-disturbance effect intensify the turbulence in the lowest atmospheric layer to form an unstable layer, which develops into the TIBL. Notably, the TIBL progressively grows from the coastline to the inland areas. The structure and dynamics of the planetary boundary layer in the ocean–continent zone during the summer period was reconstructed from lidar sounding data [49]. The TIBL is always associated with a sea breeze, so the meteorological factors that can be used include wind speed, wind direction, air temperature, relative humidity, and precipitation. On the other hand, the height of the TIBL can be considered as the height of the shallow convective boundary layer [50,51]. In the previous study, a TIBL forms if the wind blows from the sea and the boundary layer height is lower

than 500 m, as indicated by the ceilometer [52]. However, as the minimum value of the BLH is about 600 m at 20 lidar sites, using the threshold value of 500 m to identify the TIBL is not reasonable. Overall, the TIBL is an important factor when considering the BLH over the coastal areas. Thus, extra efforts must be made to select or screen the cases of TIBL, such as obtaining meteorological data, determining the direction of sea breeze, and setting the threshold value, for example, to 500 m for different stations. Finally, all this work will be conducted in the near future with enough time.

Due to the limited number of lidar observation sites, the quality of the ECMWFs-derived BLHs is still under investigation. We will perform further evaluations for as long as more ground-based lidar observations are available. Special attention should be paid when using the ECMWFs BLH over coastal areas and mountain areas.

Author Contributions: Z.Z.: methodology, software, writing—original draft, and supervision; L.M.: methodology, editing, and supervision; C.L.: data curation, investigation. All authors have read and agreed to the published version of the manuscript.

Funding: This research was funded by the National Natural Science Foundation of China, grant number 41975019.

Institutional Review Board Statement: Not applicable.

Informed Consent Statement: Not applicable.

Data Availability Statement: Lidar data were provided by courtesy of AD-Net (<http://www-lidar.nies.go.jp/AD-Net>, accessed on 23 November 2022). The ECMWFs reanalysis data are accessible via <http://apps.ecmwf.int/datasets/data/interim-full-moda/levtype=sfc/>, accessed on 23 November 2022.

Acknowledgments: The authors gratefully acknowledge the anonymous reviewers for their excellent comments and efforts. The authors would like to thank AD-Net and the ECMWFs for providing the data used in our analysis.

Conflicts of Interest: The authors declare no conflict of interest.

References

1. Arya, S.P. *Introduction to Micrometeorology*, 2nd ed.; Academic Press: Cambridge, MA, USA, 2001; pp. 1–450.
2. Stull, R.B. *An Introduction to Boundary Layer Meteorology*; Kluwer Academic Publishers: Dordrecht, The Netherlands, 1988; pp. 1–27.
3. Wood, R. Stratocumulus clouds. *Mon. Weather Rev.* **2011**, *140*, 2373–2423. [\[CrossRef\]](#)
4. Seibert, P.; Beyrich, F.; Gryning, S.E.; Joffre, S.; Rasmussen, A.; Tercier, P. Review and intercomparison of operational methods for the determination of the mixing height. *Atmos. Environ.* **2000**, *34*, 1001–1027. [\[CrossRef\]](#)
5. Seidel, D.J.; Ao, C.O.; Li, K. Estimating climatological planetary boundary layer heights from radiosonde observations: Comparison of methods and uncertainty analysis. *J. Geophys. Res.-Atmos.* **2010**, *115*, D16113. [\[CrossRef\]](#)
6. Guo, J.; Deng, M.; Lee, S.S.; Wang, F.; Li, Z.; Zhai, P.; Liu, H.; Lv, W.; Yao, W.; Li, X. Delaying precipitation and lightning by air pollution over the Pearl River Delta. Part I: Observational analyses. *J. Geophys. Res.-Atmos.* **2016**, *121*, 6472–6488. [\[CrossRef\]](#)
7. Vogelesang, D.H.P.; Holtslag, A.A.M. Evaluation and model impacts of alternative boundary-layer height formulations. *Bound.-Lay. Meteorol.* **1996**, *81*, 245–269. [\[CrossRef\]](#)
8. Hennemuth, B.; Lammert, A. Determination of the atmospheric boundary layer height from radiosonde and lidar backscatter. *Bound.-Lay. Meteorol.* **2006**, *120*, 181–200. [\[CrossRef\]](#)
9. Sawyer, V.; Li, Z. Detection, variations and intercomparison of the planetary boundary layer depth from radiosonde, lidar and infrared spectrometer. *Atmos. Environ.* **2013**, *79*, 518–528. [\[CrossRef\]](#)
10. Beyrich, F. Mixing height estimation from sodar data—a critical discussion. *Atmos. Environ.* **1997**, *31*, 3941–3953. [\[CrossRef\]](#)
11. Eresmaa, N.; Karppinen, A.; Joffre, S.M.; Räsänen, J.; Talvitie, H. Mixing height determination by ceilometer. *Atmos. Chem. Phys.* **2006**, *6*, 1485–1493. [\[CrossRef\]](#)
12. Dai, C.; Wang, Q.; Kalogiros, J.A.; Lenschow, D.H.; Gao, Z.; Zhou, M. Determining boundary-layer height from aircraft measurements. *Bound.-Lay. Meteorol.* **2014**, *152*, 277–302. [\[CrossRef\]](#)
13. Chan, K.M.; Wood, R. The seasonal cycle of planetary boundary layer depth determined using cosmic radio occultation data. *J. Geophys. Res.-Atmos.* **2013**, *118*, 12422–12434. [\[CrossRef\]](#)
14. Liu, J.J.; Huang, J.P.; Chen, B.; Zhou, T.; Yan, H.R.; Jin, H.C.; Huang, Z.W.; Zhang, B.D. Comparisons of PBL heights derived from CALIPSO and ECMWF reanalysis data over China. *J. Quant. Radiat. Transf.* **2015**, *153*, 102–112. [\[CrossRef\]](#)

15. Zhang, W.; Guo, J.; Miao, Y.; Liu, H.; Zhang, Y.; Li, Z.; Zhai, P. Planetary boundary layer height from CALIOP compared to radiosonde over China. *Atmos. Chem. Phys.* **2016**, *16*, 9951–9963. [\[CrossRef\]](#)
16. Wang, L.; Schöck, M.; Chanan, G.A. Atmospheric turbulence profiling with SLODAR using multiple adaptive optics wavefront sensors. *Appl. Optics* **2008**, *47*, 1880–1892. [\[CrossRef\]](#) [\[PubMed\]](#)
17. Kovadlo, P.G.; Shikhovtsev, A.Y.; Kopylov, E.A.; Kiselev, A.V.; Russkikh, I.V. Study of the optical atmospheric distortions using wavefront sensor data. *Russ. Phys. J.* **2021**, *63*, 1952–1958. [\[CrossRef\]](#)
18. Wilson, R.W. SLODAR: Measurement of the height of optical turbulence using the Shaka-Hartman wavefront sensor. *Mon. ne. R. Astron. Soc.* **2002**, *337*, 103–108. [\[CrossRef\]](#)
19. Shikhovtsev, A.Y. A method of determining optical turbulence characteristics by the line of sight of an astronomical telescope. *Atmos. Ocean Opt.* **2022**, *35*, 303–309. [\[CrossRef\]](#)
20. Nishizawa, T.; Sugimoto, N.; Matsui, I.; Shimizu, A.; Hara, Y.; Itsushi, U.; Yasunaga, K.; Kudo, R.; Kim, S.W. Ground-based network observation using Mie-Raman lidars and multi-wavelength Raman lidars and algorithm to retrieve distributions of aerosol components. *J. Quant. Spectrosc. Radiat. Transf.* **2017**, *188*, 79–93. [\[CrossRef\]](#)
21. Nishizawa, T.; Sugimoto, N.; Matsui, I.; Shimizu, A.; Higurashi, A.; Jin, Y. The Asian dust and aerosol lidar observation network (AD-Net): Strategy and progress. In Proceedings of the 27th International Laser Radar Conference, New York, NY, USA, 5–10 July 2015. [\[CrossRef\]](#)
22. Sugimoto, N.; Nishizawa, T.; Liu, X.; Matsui, I.; Shimizu, A.; Zhang, Y.; Kim, Y.J.; Li, R.; Liu, J. Continuous Observations of Aerosol Profiles with a Two-Wavelength Mie-Scattering Lidar in Guangzhou in PRD2006. *J. Appl. Meteorol. Clim.* **2009**, *48*, 1822–1830. [\[CrossRef\]](#)
23. Sugimoto, N.; Nishizawa, T.; Shimizu, A.; Matsui, I.; Jin, Y.; Higurashi, A.; Uno, I.; Hara, Y.; Yumimoto, K.; Kudo, R. Continuous observations of atmospheric aerosols across East Asia. *SPIE Newsroom* **2015**. [\[CrossRef\]](#)
24. Shimizu, A.; Nishizawa, T.; Jin, Y.; Kim, S.W.; Wang, Z.F.; Batdorj, D.; Sugimoto, N. Evolution of a lidar network for tropospheric aerosol detection in East Asia. *Opt. Eng.* **2016**, *56*, 031219. [\[CrossRef\]](#)
25. Sugimoto, N.; Uno, I.; Nishikawa, M.; Shimizu, A.; Matsui, I.; Dong, X.; Chen, Y.; Quan, H. Record heavy Asian dust in Beijing in 2002: Observations and model analysis of recent events. *Geophys. Res. Lett.* **2003**, *30*, 1640. [\[CrossRef\]](#)
26. Shimizu, A.; Sugimoto, N.; Matsui, I.; Arao, K.; Uno, I.; Murayama, T.; Kagawa, N.; Aoki, K.; Uchiyama, A.; Yamazaki, A. Continuous observations of Asian dust and other aerosols by polarization lidars in China and Japan during ACE-Asia. *J. Geophys. Res.-Atmos.* **2004**, *109*, D19S17. [\[CrossRef\]](#)
27. Seidel, D.J.; Zhang, Y.; Beljaars, A.; Golaz, J.-C.; Jacobson, A.R.; Medeiros, B. Climatology of the planetary boundary layer over the continental United States and Europe. *J. Geophys. Res.-Atmos.* **2012**, *117*, D17106. [\[CrossRef\]](#)
28. Han, B.; Zhou, T.; Zhou, X.; Fang, S.; Huang, J.; He, Q.; Huang, Z.; Wang, M. A new algorithm of atmospheric boundary layer height determined from polarisation lidar. *Remote Sens.* **2022**, *14*, 5436. [\[CrossRef\]](#)
29. Zhang, M.; Tian, P.; Zeng, H.; Wang, L.; Liang, J.; Cao, X.; Zhang, L. A comparison of wintertime atmospheric boundary layer heights determined by tethered balloon soundings and lidar at the site of SACOL. *Remote Sens.* **2021**, *13*, 1781. [\[CrossRef\]](#)
30. Guo, J.; Miao, Y.; Zhang, Y.; Liu, H.; Li, Z.; Zhang, W.; He, J.; Lou, M.; Yan, Y.; Bian, L.; et al. The climatology of planetary boundary layer height in China derived from radiosonde and reanalysis data. *Atmos. Chem. Phys.* **2016**, *16*, 1330–13319. [\[CrossRef\]](#)
31. Zhang, H.; Zhang, X.; Li, Q.; Cai, X.; Fan, S.; Song, Y.; Hu, F.; Che, H.; Quan, J.; Kang, L.; et al. Research progress on estimation of atmospheric boundary layer height. *Acta Meteorol. Sin.* **2020**, *78*, 522–536. [\[CrossRef\]](#)
32. Palm, S.P.; Benedetti, A.; Spinhirne, J. Validation of ECMWF global forecast model parameters using GLAS atmospheric channel measurements. *Geophys. Res. Lett.* **2005**, *32*, 109–127. [\[CrossRef\]](#)
33. Shimizu, A.; Sugimoto, N.; Matsui, I. Detailed description of data processing system for lidar network in East Asia. In Proceedings of the 25th International Laser Radar Conference, St. Petersburg, Russia, 5–9 July 2010.
34. Korhonen, K.; Giannakaki, E.; Mielonen, T.; Pfüller, A.; Laakso, L.; Vakkari, V.; Baars, H.; Engelmann, R.; Beukes, J.P.; Van Zyl, P.G.; et al. Atmospheric boundary layer top height in South Africa: Measurements with lidar and radiosonde compared to three atmospheric models. *Atmos. Chem. Phys.* **2014**, *14*, 4263–4278. [\[CrossRef\]](#)
35. New, M.; Hulme, M.; Jones, P. Representing Twentieth-Century Space-Time Climate Variability. Part II: Development of 1901–96 Monthly Grids of Terrestrial Surface Climate. *J. Clim.* **2000**, *13*, 2217–2238. [\[CrossRef\]](#)
36. Wood, R.; Bretherton, C.S. Boundary layer depth, entrainment, and decoupling in the cloud-capped subtropical and tropical marine boundary layer. *J. Clim.* **2004**, *17*, 3576–3588. [\[CrossRef\]](#)
37. Edwards, J.M.; Beljaars, A.C.M.; Holtslag, A.A.M.; Lock, A.P. Representation of Boundary-Layer Processes in Numerical Weather Prediction and Climate Models. *Bound.-Lay. Meteorol.* **2020**, *177*, 511–539. [\[CrossRef\]](#)
38. Kursinski, E.R.; Hajj, G.A.; Schofield, J.T.; Linfield, R.P.; Hardy, K.R. Observing Earth’s atmosphere with radio occultation measurements using the Global Positioning System. *J. Geophys. Res.-Atmos.* **1997**, *102*, 23429–23465. [\[CrossRef\]](#)
39. Hajj, G.A.; Ao, C.O.; Iijima, B.A.; Kuang, D.; Kursinski, E.R.; Mannucci, A.J.; Meehan, T.K.; Romans, L.J.; Juarez, M.D.; Yunk, T.P. Champ and SAC-C atmospheric occultation results and intercomparisons. *J. Geophys. Res.-Atmos.* **2003**, *109*, D06109. [\[CrossRef\]](#)
40. Tang, G.; Zhang, J.; Zhu, X.; Song, T.; Münkel, C.; Hu, B.; Schäfer, K.; Liu, Z.; Zhang, J.; Wang, L.; et al. Mixing layer height and its implications for air pollution over Beijing, China. *Atmos. Chem. Phys.* **2016**, *16*, 2459–2475. [\[CrossRef\]](#)
41. Zhou, T.; Xie, H.; Bi, J.; Huang, Z.; Huang, J.; Shi, J.; Zhang, B.; Zhang, W. Lidar measurements of dust aerosols during three field campaigns in 2010, 2011 and 2012 over Northwestern China. *Atmosphere* **2018**, *9*, 173. [\[CrossRef\]](#)

42. Zhang, Z.; Huang, J.; Chen, B.; Yi, Y.; Liu, J.; Bi, J.; Zhou, T.; Huang, Z.; Chen, S. Three-year continuous observation of pure and polluted dust aerosols over northwest China using the ground-based lidar and sun photometer data. *J. Geophys. Res.-Atmos.* **2019**, *124*, 1118–1131. [[CrossRef](#)]
43. Sugimoto, N.; Jin, Y.; Shimizu, A.; Nishizawa, T.; Yumimoto, K. Transport of mineral dust from africa and middle east to east asia observed with the lidar network (AD-Net). *SOLA* **2019**, *15*, 257–261. [[CrossRef](#)]
44. Qi, S.; Huang, Z.; Ma, X.; Huang, J.; Zhou, T.; Zhang, S.; Dong, Q.; Bi, J.; Shi, J. Classification of atmospheric aerosols and clouds by use of dual-polarization lidar measurements. *Optics Express*. **2021**, *29*, 23461–23476. [[CrossRef](#)]
45. Honda, N.; Coulibaly, S.; Funasaka, K.; Kido, M.; Oro, T.; Shimizu, A.; Matsumoto, T.; Watanabe, T. Comparison of the concentration of suspended particles and their chemical composition near the ground surface and dust extinction coefficient by Lidar. *Biol. Pharm. Bull.* **2022**, *45*, 709–719. [[CrossRef](#)] [[PubMed](#)]
46. Zhang, S.; Huang, Z.; Li, M.; Shen, X.; Wang, Y.; Dong, Q.; Bi, J.; Zhang, J.; Li, W.; Li, Z.; et al. Vertical structure of dust aerosols observed by a ground-based raman lidar with polarization capabilities in the center of the Taklimakan desert. *Remote Sens.* **2022**, *14*, 2461. [[CrossRef](#)]
47. Su, T.; Li, Z.; Kahn, R. A new method to retrieve the diurnal variability of planetary boundary layer height from lidar under different thermodynamic stability conditions. *Remote Sens. Environ.* **2020**, *237*, 111519. [[CrossRef](#)]
48. Odintsov, S.L.; Gladkikh, V.A.; Kamardin, A.P.; Nevzorova, I.V. The height of the region of intense turbulent heat transfer in a stably stratified boundary layer of the atmosphere. Part 2: Relationship with surface meteorological parameters. *Atmos Ocean Opt.* **2021**, *34*, 117–127. [[CrossRef](#)]
49. Pavlov, A.N.; Shmirko, K.A.; Stolyarchuk, S.Y. Features of the structure and dynamics of the planetary boundary layer in the Ocean-continent zone. Part II. Summer period. *Atmos Ocean Opt.* **2013**, *26*, 285–292. [[CrossRef](#)]
50. Prabha, T.V.; Venkatesan, R.; Mursch-Radlgruber, E.; Rengarajan, G.; Jayanthi, N. Thermal internal boundary layer characteristics at a tropical coastal site as observed by a mini-SODAR under varying synoptic conditions. *J. Earth Syst. Sci.* **2002**, *111*, 63–77. [[CrossRef](#)]
51. Sicard, M.; Pérez, C.; Rocadenbosch, F.; Baldasano, J.M.; García-Vizcaino, D. Mixed-layer depth determination in the barcelona coastal area from regular lidar measurements: Methods, results and limitations. *Boundary-Layer Meteorol.* **2006**, *119*, 135–157. [[CrossRef](#)]
52. Wei, J.; Tang, G.; Zhu, X.; Wang, L.; Liu, Z.; Cheng, M.; Münkel, C.; Li, X.; Wang, Y. Thermal internal boundary layer and its effect on air pollutants during summer in a coastal city in North China. *J. Environ. Sci.* **2018**, *70*, 37–44. [[CrossRef](#)]